Ground-Penetrating Radar Modeling Across the Jezero Crater Floor

Sigurd Eide, Svein-Erik Hamran, Henning Dypvik, and Hans E. F. Amundsen

***Abstract*—This article assesses how the ground-penetrating radar RIMFAX will image the crater floor at the Mars 2020 landing site, where lithological compositions and stratigraphic relationships are under discussion prior to mission operation. A putative mafic unit (lava flow, volcanic ash, or volcaniclastic deposit) on the crater floor will be crucial in piecing together the chronology of deposition and for understanding the volcanic history in the region. In order to see how lithological properties and subsurface geometries affect radar sounding, a synthetic radargram is generated through forward modeling with a finite-difference time-domain method. The acquisition is simulated across the mafic unit as a succession of lava flows, exploring detection of internal structures and contacts to adjacent lithologies. To compare modeling results with the alternative formation scenarios, a discussion about sounding over a tephra or volcaniclastic material is presented. Similarities and differences between Martian and terrestrial lithologies can be related to electromagnetic properties relevant for radar sounding. This article, therefore, evaluates potential scientific insights gained from acquisition across the disputed mafic unit, in light of proposed hypotheses of lithological generation.**

***Index Terms*—Finite-difference time-domain (FDTD), ground-penetrating radar (GPR), mars 2020, RIMFAX.**

I. Introduction

DISCLOSING the near-surface geology will be among the great advances in future exploration of Mars. Not only will it add to our understanding of the planet's geological history and *in situ* resources, but it may also be of major astrobiological interest [1]. The radar imager for Mars' subsurface experiment (RIMFAX) [2] aboard NASA's Mars 2020 rover mission will pioneer in imaging the Martian near surface. The ground-penetrating radar (GPR) will take measurements every 10 cm along the drive path, unveiling subsurface structures, bedding, and stratigraphic relationships. In like manner, GPRs are also included among the scientific payloads for the Chinese Tianwen-1 mission [3] (launched in 2020) and the upcoming European-Russian ExoMars mission [4] (planned for launch in 2022). Improved understanding of Martian geology will be achieved through radar sounding during the next decade of Martian exploration.

To image the subsurface, a GPR transmits microwaves to detect changes in density and composition, i.e., variations in the ground's electromagnetic properties. In those terms, lithological properties can be described by the relative dielectric constant ε^*

$$\varepsilon^* = \varepsilon' - j\varepsilon''. \tag{1}$$

The real part ε' is referred to as the dielectric constant and dominates the propagation velocity in a medium. A GPR essentially records reflections caused by velocity differences in the subsurface, e.g., at the interface between two distinct lithologies. However, small-scale heterogeneous velocity changes can cause scattering and lead to energy reduction in the propagating wavefront, denoted by volume losses. The imaginary part ε'' is referred to as the dielectric loss factor and is a frequency-dependent quantity ($\varepsilon'' = \sigma/\omega\varepsilon_0$, where ω is the angular frequency of the electromagnetic wave, σ is the medium conductivity, and ε_0 is the permittivity of vacuum). The dielectric loss factor describes the intrinsic attenuation in a medium that greatly affects penetration depths in radar sounding. Magnetic properties will similarly influence propagation velocities and attenuation but are generally negligible with the exception of lithologies containing substantial amounts of ferro- or ferrimagnetic material.

Investigation in terrestrial and lunar terrains is a starting point for predicting the dielectric properties for unexplored lithologies on Mars and assessing similarities and differences for radar sounding. As on Earth, GPR imaging has proven successful for several geological applications, including stratigraphic analysis [5] and sounding in volcanic terrain [6], [7]. Landed missions on the Moon have used radar sounding to investigate the regolith thickness and volcanic layering [8]–[10]. Laboratory measurements of dry rocks show wide variations in dielectric constants with a strong correlation to bulk density [11]–[13]. While water content greatly increases the attenuation of microwaves, the dielectric loss factor in dry rocks is dominated by the number of chemical constituents as titanium and iron oxides [12], [13].

In contrast, on Mars, direct measurements of the dielectric constant have only been done by the Phoenix lander [14], but Martian soil simulants have been extensively analyzed in the laboratory [15] and GPR field tests have been conducted in Mars analog terrain [16], [17]. Intriguingly, prominent magnetic surface properties have been measured *in situ* by several landed missions [18]–[20], and magnetization in the lithosphere has been mapped from orbit and, at places, estimated to be one

Manuscript received October 30, 2020; accepted January 27, 2021. Date of publication February 1, 2021; date of current version February 22, 2021. *(Corresponding author: Sigurd Eide.)*

Sigurd Eide and Svein-Erik Hamran are with the Department of Technology Systems, University of Oslo, 2007 Kjeller, Norway (e-mail: sigurd.eide@its.uio.no; s.e.hamran@its.uio.no).

Henning Dypvik is with the Department of Geosciences, University of Oslo, 0371 Oslo, Norway (e-mail: henning.dypvik@geo.uio.no).

Hans E. F. Amundsen is with the Vestfonna Geophysical AS, 8310 Kabelvåg, Norway (e-mail: ha@epx.no).

Digital Object Identifier 10.1109/JSTARS.2021.3055944

order of magnitude larger than on Earth [21]. It is, therefore, possible that magnetic properties could be noticeable for radar sounding on Mars. In the region around the Mars 2020 landing site, specifically, the mapped crustal magnetization is weak [22], although it does not preclude substantial magnetic mineralogy in a demagnetized crust or localized magnetization that is undetectable at orbital altitudes.

Space-borne radars have been sounding the Martian crust's upper hundreds to thousands of meters [23], [24], operating at lower frequencies and larger spatial scales compared to RIMFAX. Analyzing recordings from Shallow Radar (SHARAD) on Mars Reconnaissance Orbiter, Morgan *et al*. [25] investigated the possibility for detecting shallow subsurface reflections that could presumably also be seen by RIMFAX. However, due to a large spatial footprint and topographic variation around the Mars 2020 landing site, clutter obscure subsurface reflections and make such correlation problematic. Accordingly, it is at present largely unknown what RIMFAX will be able to image when operating on the surface of Mars.

As a precursor to planetary rover missions, orbital data are used for geological investigations. Despite extensive mapping already having been conducted at the Mars 2020 landing site [26]–[29], it is generally hard to infer from orbit the origins and exact relationships between outcrops [30], [31], let alone their relationship in the subsurface. Consequently, predicting how the subsurface geology will be imaged by a ground-based GPR holds room for considerable conjecture, while all the more important for evaluating potential science outcome from the upcoming acquisition. To assess RIMFAX-imaging based on the available information, a workflow for generating synthetic radargrams through forward modeling will be presented.

A putative lava flow [26], [32], in this article referred to as the mafic unit, is covering large areas of the landing site; however, based on orbital data alone, it is not possible to rule out alternative origins such as tephra or volcaniclastic deposition [29], [33]. Determining its formation history and stratigraphic context will be central for understanding the geological history of the area. After reviewing discussions surrounding the landing site geology, radar sounding will be simulated in order to examine possible detections made within and beneath the hypothesized lava flow and identify their scientific implications. Similarities and differences between electromagnetic properties in Martian and terrestrial lithologies will be explored, and comparisons will be done between the proposed formational hypotheses for the mafic unit.

II. Modeling Workflow

To assess GPR-acquisition in frontier areas where information is sparse, a modeling workflow was developed (see Fig. 1). Geological mapping and interpretations build on previous studies of the landing site extend the geological model into the subsurface. Using the software BGS Groundhog Desktop GSIS [34] for constructing the subsurface model, dimensions and geometries are kept consistent with observations made of the surface and their geological interpretations. Electromagnetic values are assigned based on interpreted formation, e.g., similar to laboratory measurements of a particular type of rock, predictions from radar sounding in comparable terrain, or rock physics considerations.

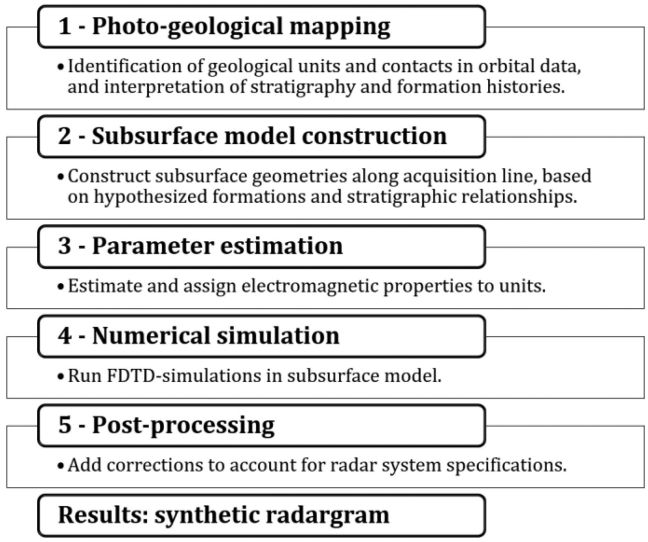

Fig. 1. Modeling workflow involves five steps for producing a synthetic radargram in a frontier area. The minimum input data required for steps 1 and 2 are surface imagery and a digital terrain model. When additional information is available, e.g., detailed surface observations, it can be included in steps 1–3 to enhance the authenticity of the input model used in numerical simulations, step 4. Step 5 corrects for the large data range achieved in numerical simulations compared to that of the actual radar system.

Numerical simulations are carried out with the software gprMax [35], employing a finite-difference time-domain (FDTD) algorithm [36] for solving Maxwell's equations in three dimensions. The amount of computational resources required in numerical simulations put restrictions upon the level of detail that can be considered and the accuracy of the results. To enable FDTD-simulation over hundreds of meters, each sounding is simulated in a separately gridded model around the source and receiver. The domain size is adjustable according to along- and cross-track contributions and target depths. The along-track dimension is predominantly 4.0 m but increases to as much as 10–15 m in areas where off-nadir reflections are thought to be prominent. In the cross-track direction, layer boundaries are extrapolated 3.0 m laterally, ensuring that the first Fresnel zone is enclosed in the domain. To replicate more natural-like surfaces, fractal surface roughness is added in both along- and cross-track directions [5], Cross-track dips of horizons due to geological structures are not accounted for. The depth dimension extends until 19 m at most.

RIMFAX's "deep operation mode" is the focus of this article, where a frequency modeled continuous wave (FMCW) sweeps through the frequency range 150–600 MHz. To prevent very large simulation times, however, an 11.0 ns broadband Ricker wavelet with 250 MHz center frequency and a frequency content that encompasses that of the FMCW is employed as a first approximation.

Discretization of the model space is constrained by the frequency content of the source wavelet, so in order to prevent substantial numerical dispersion, discretization needs to be at least

ten times smaller than the smallest wavelength [37]. However, targets in the model for the most part are substantially thick and laterally continuous and not considered to put significant constraints upon discretization. For the highest value of the dielectric constant in this article ($\varepsilon' = 6.0$), the wavelength corresponding to 600 MHz is sampled by ten cells when discretization of Yee-cells [36] is 0.02 m^3. The CFL-condition ensuring a stable numerical process [37] requires a corresponding time step of 3.8e-11 s. A 250 MHz Ricker wavelet has a highest significant frequency at 700 MHz (at its -40 dB level), giving an estimated largest physical phase-velocity error of -1.5% [38].

In the deep operation mode, gating between transmission and recording in FMCW-acquisition efficiently mutes reflections within the upper meter, and therefore, the shallow range is not considered in this article (but still included in the simulation results for maintaining context between the modeled radargram and surface imagery). Accordingly, a Hertzian-dipole radiation source is considered appropriate for imaging deep structures close to nadir direction, instead of employing an elaborate antenna model. Reception is also done at a single Yee-cell, separated by ten cells from the source.

In post-processing, corrections are made for a presumed 150 dB system dynamic range (SDR) for RIMFAX. Evaluating the signal-to-noise ratio (SNR) from the radar equation, SDR is defined to encompass the system-specific parameters [39], as in

$$\mathrm{SNR} \approx \mathrm{SDR} \times \left[\frac{\lambda_0^2 \, e^{-4(\alpha_i + \alpha_v)(R - R_s)} \, T_s^{\downarrow} \, T_s^{\uparrow} \, \Gamma_{\mathrm{target}}}{(4\pi)^2 (2R)^2} \right]. \quad (2)$$

The last term contains variables related to geometrical spreading (R = range), medium properties (α_i = intrinsic attenuation, α_v = volume loss), transmission losses along the propagation path (T_S = surface transmission), reflection at the target (Γ_{target}= target reflectivity), as well as the wavelength in free air (λ_0), and the antenna height above ground (R_S). Transmission at the surface is included because the antenna is air-coupled and mounted 60 cm above the ground. The approximate equality in (2) derives from a near-nadir approximation with normal incidences at plane, specular boundaries, enabling the target to be expressed in terms of the Fresnel reflectivity [40].

During numerical simulations, parameters in the last term of (2) are accounted for through the FDTD solution of Maxwell's equations, while the radar system parameters are not included. To imitate RIMFAX' detection limit, signals below the SDR are concealed by setting a fictive noise level (N_0) according to a matched filter receiver

$$\frac{P_t}{N_0/2} \approx \mathrm{SDR} \rightarrow \; N_0 \approx \frac{2P_t}{\mathrm{SDR}}, \quad (3)$$

where P_t is the power of the transmitted pulse. Fig. 2 presents a schematic overview of the deep operation mode and signal levels that are simulated.

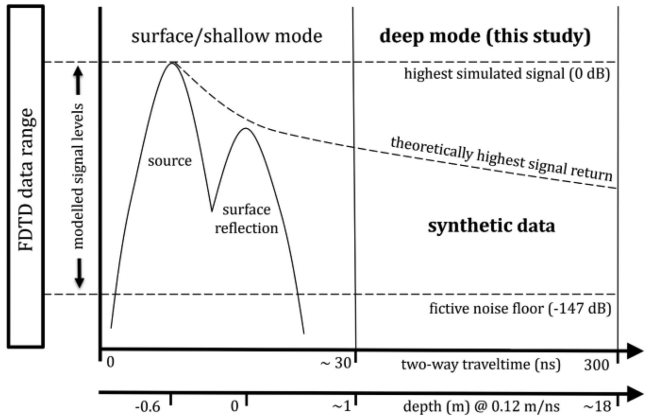

Fig. 2. Schematic view of modeled radar acquisition. The upper meter (∼30 ns) containing the transmitted wave, surface reflection, and other shallow reflections is not considered in the deep mode due to gating in FMCW acquisition. Total recording length is set to 300 ns (∼18 m at 0.12 m/ns). Left axes display how simulated signal levels fall within the FDTD data range. Simulated signal levels below -147 dB are muted, according to the presumed detection limit for RIMFAX (SDR = 150 dB). The synthetic radargram will consist of data bounded by the fictive noise floor and a theoretically highest signal return due to geometrical spreading.

III. Surface and Subsurface Models

A. Geological Setting

Jezero crater ($D = 50$ km), selected as the landing site for the Mars 2020 mission, is located in the Nili Fossae region on the northwestern edge of the ∼3.9 Ga Noachian-aged Isidis impact basin ($D = 1900$ km) [41], [42]. Extensive breccias and impact melts have been noted in the area [43], [44] as well as younger fluvial channels [45] and mineralogical composition indicating early aqueous alteration [46]–[48]. To the west is the Hesperian-aged volcanic complex of Syrtis Major Planum, with possible lava flows extending into the Nili Fossae region [49].

Jezero is a complex impact crater with a central peak [50] that has been severely eroded. Large amounts of scree, mass flows, density current, and melt rock most likely formed during the crater excavation and various stages of modification, comparable to terrestrial impacts where the aqueous origin is still discussed [51], [52]. Based on general depth/diameter ratios for complex craters [53], Jezero may have experienced a ∼1 km thick post-impact succession [32], [54].

Light-toned outcrops are present on the Jezero crater floor, displaying a rough surface expression with varying topography and polygonal fractures at a variety of scales. This lithology has been interpreted to be the lowest visible unit among the post-impact deposits in Jezero Crater [26], [32] and has been called various names in the published literature; however, in this article, it is referred to as the light-toned floor (LTF). Olivine and Mg-carbonate signatures are detected in visible to near-infrared (VNIR) reflectance spectra of this unit [26], [54], and possibly related to regional carbonate-bearing exposures observed more broadly in the Nili Fossae region [26], [29]. A summary of formation scenarios is found in [55] and references therein.

Most likely in late Noachian time, a closed basin with standing water was contained within the crater, which later developed

into a hydrologically open lake [45]. Two possible inlet valleys entering the crater through the northern and western rims were feeding the lake system, while a breach in the eastern rim formed the major outlet. Located at the mouth of each inlet valley are deeply eroded deltaic deposits still present with a morphology reminding of fluvial-dominated deltas [32], [45]. These were deposited on top of the LTF [26], [54]. Phyllosilicates and carbonaceous material detected in VINR data indicate early aqueous alteration [54], likely due to detrital deposited material sourced from the nearby Noachian terrain [26].

B. Disputed Mafic Unit

Interpreted to be the youngest consolidated lithology in Jezero, the relatively flat and dark-toned mafic unit appears to onlap older strata within Jezero crater [26], [32]. It displays varying morphological expressions, ranging from smooth to rough, that may be caused by a nonuniform distribution of a mantling material, possibly unconsolidated, overlying the unit's more cratered surfaces [27], [28], whereas Kah *et al*. [56] proposed that the variation in smoothness reflects a sporadic thin veneer of dark-toned material, mantling the underlying rough LTF.

VNIR spectra of the unit show mafic mineralogy (olivine and pyroxene content), which indicates a possible volcanic origin [26], [33]. Morphological observations supporting a low-viscous lava flow origin are a relatively smooth and flat crater-retaining surface and lobating margins embaying neighboring outcrops [26], [32]. As noted by several authors [29], [33], however, alternative formational hypothesizes as a tephra or volcanoclastic deposit cannot be ruled out based on orbital observations alone, in particular, due to similarities between the mafic unit on the crater floor and a regional unit on the rim and outside of Jezero crater.

Based on crater counting, estimated ages for the mafic unit range from 3.45 Ga in the Neukum system [57] to 2.6 Ga [58] and 1.4 Ga [32] in the Hartmann system. However, Cofield and Stack [27] emphasized that caution needs to be applied in case the unit is covered by a thin mantle, and age estimates may only be correct in certain areas. Kah *et al*. [56] advocated that a thin mantle of dark-toned material could be transparent to older craters retained from the underlying LFT, not the mafic unit itself.

Schon *et al*. [32] proposed emplacement of the mafic unit posterior to the cessation of fluvial activity, suggesting the delta was partially eroded prior to possible volcanic emplacement. This is consistent with Goudge *et al*. [57] who studied volcanic resurfacing in Martian open-basin lakes and found no evidence of water interaction in the Jezero crater. Furthermore, buffered crater counts along the valleys that once fed the Jezero paleolake indicate that the fluvial system seceded in late Noachian $\sim$3.8 Ga in the Neukum system [59]. Contrarily, Ruff [60] suggested inverse stratigraphic relationships due to the lack of erosional contact toward the delta deposits. Alternatively, Ruff [60] also indicated that this could be caused by a delta unit less prone to erosion than the mafic material. Explaining this discrepancy, Horgan *et al*. [33] advocated a more interfingered relationship, where parts of the delta could have been deposited after emplacement of the mafic unit.

The vertical extent of the mafic unit is largely unknown, although several thickness estimates have been made along its margins: Schon *et al*. [32] estimated 10–30 m, Goudge, *et al*. [26] estimated $<$ 10 m, and Shahrzad *et al*. [58] estimated $\sim$13 m. Furthermore, in the proposed scenario with the mafic unit as a thin mantling layer, Kah *et al*. [56] suggest that measuring the escarpment height only demonstrates minimum erosion of the LTF along the margins. The mafic unit may have acted as a cap, while topographically higher and previously uncovered parts of the LTF have eroded, resulting in the apparent erosional embayment structure.

C. Acquisition Traverse and Subsurface Model

A selected traverse across the mafic unit runs close to the nominal mission traverse [61] and includes several geological units identified from orbital observations. The traverse is presented in Fig. 3(a), plotted on top of orbital imagery from Dickson *et al*. [62]. To the SSE is the LTF with a rough surface expression and varying relief. The line extends across the darker toned and relatively flat mafic unit, where a range of distinct surface expressions can be seen to the east and west of the line, from smooth to rough. Here, it also crosses over a 2-m wide linear fracture and a 10-m diameter sized impact crater. Toward the NNW, the line approaches $\sim$50-m tall erosional scarp of the western delta deposits.

A hypothesized subsurface model is constructed along the traverse, with the mafic unit modeled as an accumulation of basaltic lava flows embaying the delta deposits and the LTF [see Fig. 3(c)]. Prodelta deposits are assumed NNW of the line based on Goudge *et al*. [63], whereas numerous formation scenarios and compositions have been proposed for the LTF. In this article, the "Comanche" outcrops in Columbia Hills are used as a proxy due to their comparable composition within VNIR constraints to exposures of carbonate-bearing rocks in the Nili Fossae region [64]. Mars Exploration Rover Spirit studied these outcrops and interpreted them to be volcaniclastics with 16 to 34 weight percent carbonaceous material, possibly cemented through hydrothermal activity.

A series of simplifications are made during the construction of the subsurface model. Presuming a general subsurface model for low latitude regions, the regolith is composed of dry sedimentary and volcanic rocks [65], [66] where attenuation of radar waves is dominated by volume losses and intrinsic losses due to Fe-/Ti-oxide content. Magnetic properties are assumed negligible and the dielectric properties are assumed uniformly distributed within each geological unit (the dielectric constant and conductivity are invariant for each unit). Temporal variations and their effect on the regolith's dielectric properties, due to temperature changes [15] or atmospheric interaction [14], [67], are not considered.

The mafic unit is ascribed typical properties of basalts ($\varepsilon' = 6$ and $\varepsilon'' = 0.25$ at the 250 MHz center frequency), supported by SHARAD-observations confirming that properties of Martian lava flows are comparable to their terrestrial and

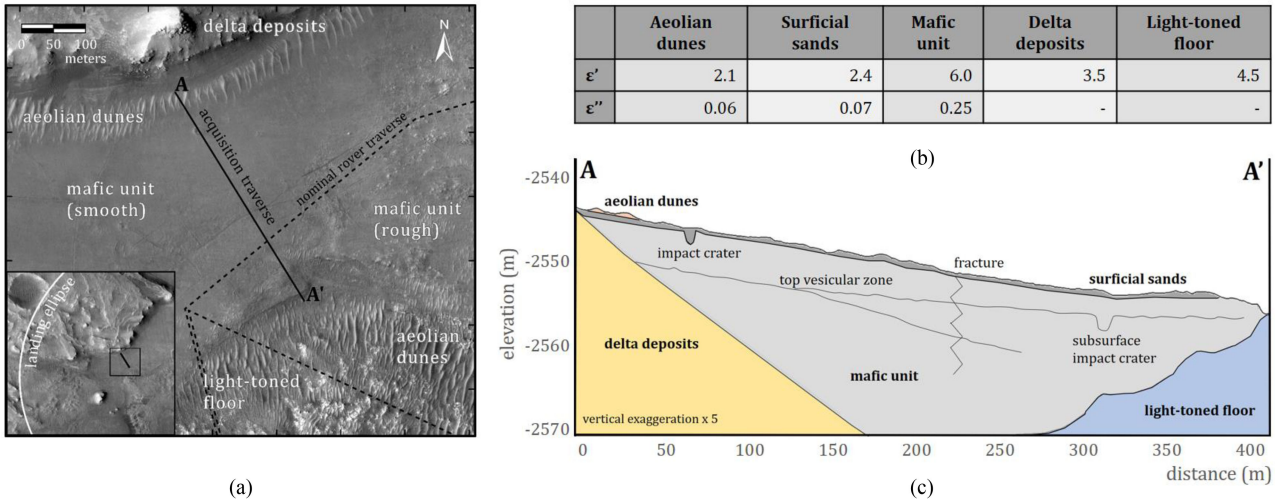

	Aeolian dunes	Surficial sands	Mafic unit	Delta deposits	Light-toned floor
ε'	2.1	2.4	6.0	3.5	4.5
ε''	0.06	0.07	0.25	-	-

Fig. 3. (a) Map with the acquisition traverse in this article (A-A': solid line) together with the nominal Mars 2020 rover traverse (dashed line). Annotations describe units identified in photogeologic mapping. The image embedded in the lower-left corner of the map gives a regional context of the map frame and acquisition traverse. (b) Parameters as defined for each unit. The dielectric loss factors are listed for the 250 MHz center frequency. (c) Schematic view of the cross-sectional model over which radar sounding is simulated.

lunar counterparts [68]. A great variety of flow morphologies exist [69], but from the crater floor's relatively flat topography and interpreted embaying features [26], [32], we assume fairly laterally homogeneous basaltic flows with the typical tripartite internal structure [70]: 1) a less dense top vesicular zone (TVZ); 2) a compact middle zone; and 3) a thin basal section with some vesicles. In the subsurface model, separate flows are divided by the TVZ with up to ∼30% porosity increase, similar to emplaced low viscous flows on Earth. This implies a decrease in the dielectric constant over this zone ($\varepsilon' = 4$–6), in agreement with the relationship to bulk density for dry rocks. The upper reflector of the TVZ is assigned ±0.5 m fractal roughness intends to replicate the surface expression of the crater floor's rougher parts, while the lower boundary is constructed with gradual and randomly decreasing porosity.

The subsurface model includes the 10 m diameter impact crater (60 m along the traverse) and 2 m wide linear fracture (220 m along the traverse), which is observed in surface imagery, as well as an idealized crater structure in the subsurface (310 m along the traverse). Both craters are constructed with a 0.2 depth/diameter ratio and with gradual and randomly varying dielectric constants in the surrounding deformation zone. The fracture is modeled similarly but as a 2-m thick vertically extending deformation zone. In all cases, dielectric properties are assigned according to a maximum ∼10% fracture induced porosity.

Sedimentary porosities will in general be higher on Mars than for terrestrial equivalents due to lower surface gravity and weakened mechanical compaction [71]. However, high amounts of cementation have been observed on Mars [72], which in turn can drastically reduce porosities. As a first estimate, rather low dielectric values are assumed for the prodelta deposits ($\varepsilon' = 3.5$) and cemented volcaniclastic rocks ($\varepsilon' = 4.5$). As only their top surfaces are considered, intrinsic and volume losses are disregarded together with any internal layering. The top surface of the LTF is generated by extrapolating its wavy surface topography into the ground, with additional ±0.5 m fractal roughness, while the delta has a smooth and dipping top surface with ±0.1 m fractal roughness. The aeolian dunes and the unconsolidated layer mantling the mafic unit are assumed to have low densities (1.1 and 1.3 g/cm^3, respectively) in the range of *in situ* measurements done by the Viking lander [73]. This corresponds to low dielectric constants ($\varepsilon' = 2.1$ and $\varepsilon' = 2.4$) and losses ($\varepsilon'' = 0.06$ and $\varepsilon'' = 0.07$, at the center frequency) according to measurements of the soil simulant JSC-1 [15].

IV. Results and Discussion

The synthetic radargram presented in Fig. 4(a) displays the simulated radar soundings where each trace has a recorded length of 300 ns (the equivalent of ∼18 m depth, assuming a constant medium velocity of 0.12 m/ns). Traces have been applied a dewow-filter and gain before stacked and corrected for time-zero and topography. The aeolian dunes and the unconsolidated layers are modeled with thicknesses up to 0.5 m, so detection of these units is not considered in the deep operation mode. They still have a great influence on underlying reflectors, as reflectors are observed shifted vertically according to the amount of low-density overburden. This is particularly apparent below the filled impact crater (60–70 m along the traverse), where imaging of the structures below is distorted [Fig. 4(b)].

Distinct reflections from layering within the mafic unit can be detected, with the TVZ (top vesicular zone) displaying a strong top reflection that grades into weaker incoherent reflections [see Fig. 4(a)–(d)]. In general, the well-known tripartite structure can be difficult to detect due to the gradual density variations within individual flows, although separate lava flows are distinguished in GPR surveys on Earth [7], [16]. In the simulation results, the TVZ-layer thickness can be inferred from the vertical extent of scattering. On Mars, acquiring such information could reveal

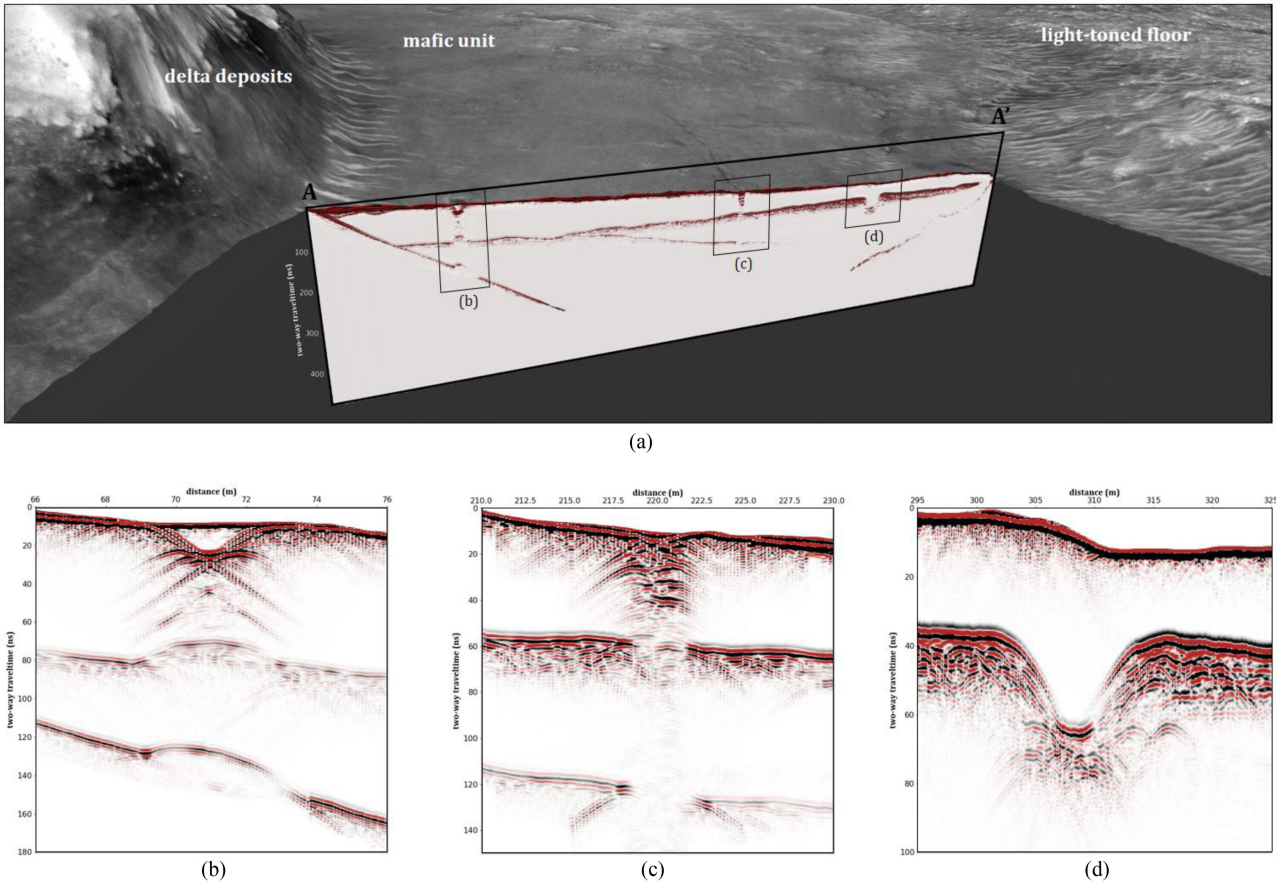

Fig. 4. (a) Synthetic radargram displays the results from modeling radar sounding over the 400 m acquisition traverse (A-A'). Note that the radargram is aligned with the topography, but its vertical axis below the surface is in two-way travel time [ns] and has a vertical exaggeration of x2.0, assuming a constant medium velocity of 0.12 m/ns. Image zooms in (a) on the impact crater, (b) on the vertical fracture, and (c) on the subsurface crater structure.

clues about paleoenvironmental conditions due to how the internal vesicularity solidifies during cooling and is affected by the confining pressure [74]. In general, the TVZ in Martian lava flows should be thinner than on Earth due to lower atmospheric pressure [75] as the distribution of vesicles within flows shows a good fit with the ideal-gas law. Confining pressure should also be prominent for lava flows emplaced in an aqueous environment, although other structures and flow morphologies could then be apparent [69]; and no evidence has been found to support fluvial and/or lacustrine activity within Jezero coeval with emplacement of the hypothesized lava flow [57]. Studying detection of TVZ-thickness in more detail, however, is outside the scope of this article, which could require comparison with a radiative-transfer model or with a GPR field survey on Earth.

Image distortion is observed where the acquisition line crosses the linear fracture (∼220 m along the traverse) [see Fig. 4(c)]. The fracture is clearly visible from the highly scattering appearance in the radargram, but its vertical extent is difficult to constrain due to high volume loss and recorded clutter. At 300–315 m along the traverse, the general shape of the subsurface crater is resolved in the simulations [see Fig. 4(d)]. The image is not a typical "bow-tie," as expected from off-nadir reflections when sounding over concave structures, but rather a collection of diffractions below the concavely shaped TVZ.

In Fig. 5(a) and (c), there are clear distinctions between the rather plane reflections of the dipping delta deposits and the rougher LTF surface, where the latter results in many diffractions collectively forming an undulating and slightly incoherent reflection. The maximum depth of detection is compared with calculations according to (2) [see Fig. 5(b) and (d)], verifying that returned signal levels are correctly simulated and within range of plane-wave theoretical estimates. Due to a large velocity difference between the crater floor and the delta deposits, detection of the top delta reflector is achievable down to ∼16 m in the simulations. A smaller velocity change toward the LTF, together with an undulating surface that further distorts imaging, makes detection possible down to ∼14 m. The discrepancy between modeling results and calculations exists as the latter does not account for a broadband source wavelet, complex overburden, volume losses through the TVZ, off-nadir reflections from dipping and rough interfaces, etc.

A. Alternative Formation Scenarios for the Mafic Unit and Implications for Radar Sounding

The character of layering within pyroclastic or volcaniclastic deposited material is very different from structures within a succession of lava flows. Radar sounding over deposited material

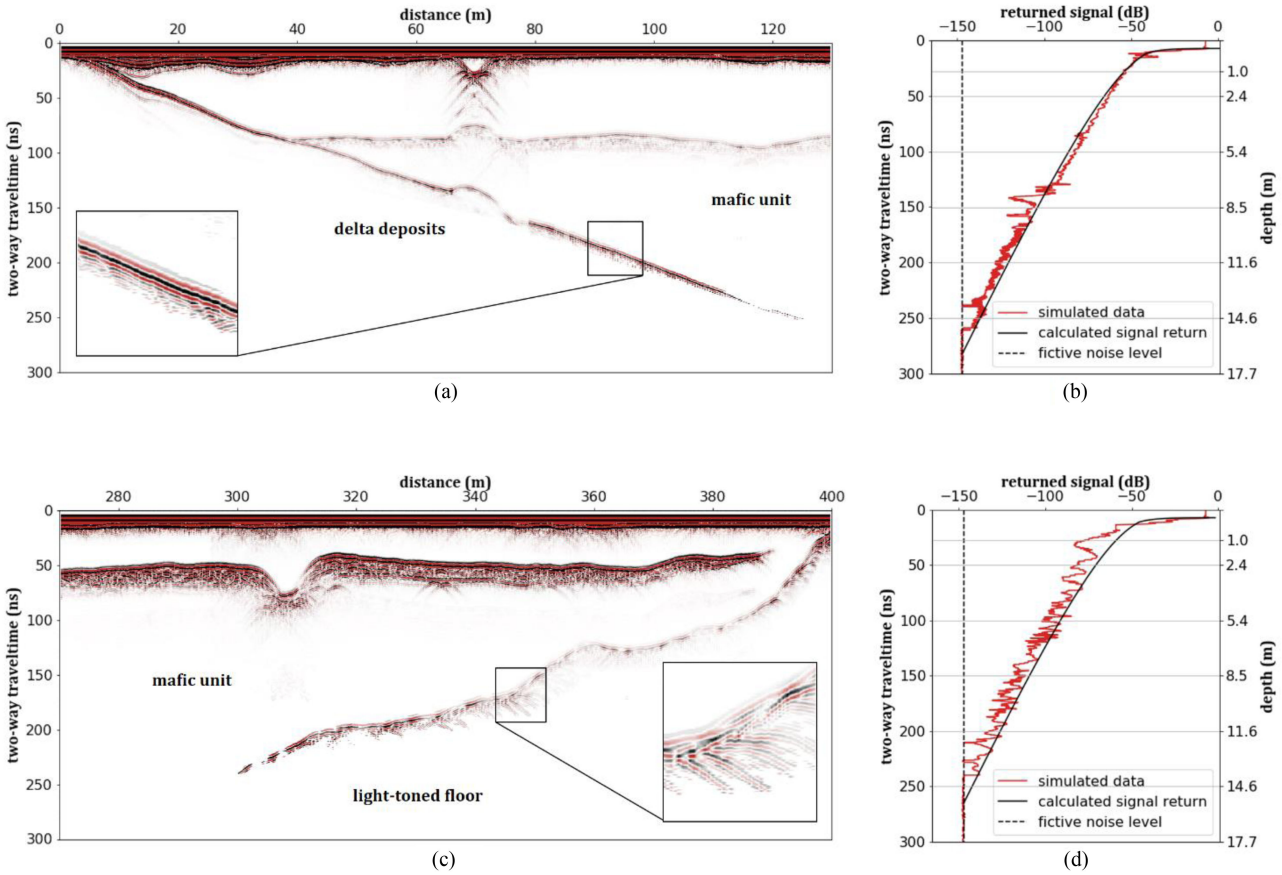

Fig. 5. Detection of lithological boundaries through the mafic unit, where left images show modeling results over the (a) delta deposits and (c) LTF unit. Radargrams are displayed in two-way traveltime below time zero. For each radargram, there is a zoomed-in window highlighting the contact. (b), (d) Corresponding signal powers (red line) measured over the reflections, plotted together with plane-wave calculations of SNR/SDR (black line) according to (2). Depth axes correspond to a constant medium velocity of 0.12 m/ns for a radar located 0.6 m above ground. The detection limit is at the -147 dB noise level defined according to (3).

can detect decimetre-scale bedding and stratigraphic geometries indicative of the depositional environment and mechanism [5]. While traversing over a pyroclastic or volcaniclastic mafic unit, RIMFAX could possibly detect individual layers based on bulk density differences and constrain corresponding bedding geometries. In the case of a pyroclastic material, GPR is furthermore capable of detecting the degree of welding/consolidation within a deposit [17], [76], which in turn could be related to the physical and thermal properties of the materials [77].

Pyroclastic deposits on Mars could be very porous, as Carter *et al*. [78] observed when studying subsurface reflections from SHARAD-sounding over the Medusae Fossae Formation. They identified possible low-density welded or interlocked pyroclastic deposits, with an estimated bulk dielectric constant of $\sim$3.0 for the formation's upper hundreds of meters. Their prediction corresponds to very high porosities despite the formation's capability of sustaining steep-sided yardangs and ridges seen in orbital imagery. In general, dry, deposited rocks on Earth will have lower densities and dielectric constants than lava flows. The low surface gravity on Mars further weakens the effect of mechanical compaction so that volcaniclastic and pyroclastic deposits are on average expected to have even lower densities. This is in contrast to Martian lava flows with electromagnetic properties similar to that of Earth and the moon, and even slightly higher due to possible reduced vesicularity. Sounding over a pyroclastic or volcaniclastic material should for that reason be affected by noticeable low dielectric values (e.g., $\varepsilon' = 3$-5) compared to sounding over lava flows with typically high values ($\varepsilon' = 6$-9), although pyroclastic welding or cementation in volcaniclastic material could increase the dielectric constant and reduce this gap.

Drawing on the experience from the space-borne radars on Mars, predicting penetration depths in front of data acquisition is very difficult due to the unknown subsurface environment [79]; so maximum penetration depths in this article (see Fig. 5) are included to verify the numerical simulations, not to give quantitative estimates. However, penetration depths depend upon overburden properties, especially the amount of intrinsic attenuation and volume losses. This implies that the characteristically lower dielectric constants expected for tephra or volcaniclastic deposits, compared to lava flows, would in general yield greater detection depths. Not considering volume losses, this prediction is valid for dry rocks where the pore space is not occupied by brine or ice, and attenuation is caused by mineral constituents in the rock (e.g., Ti/Fe-oxide content). That is, intrinsic attenuation for a dry porous rock ($\alpha_i = \pi\varepsilon''/\omega\sqrt{\varepsilon'}$; low-loss approximation

for $\varepsilon''/\varepsilon' << 1$) will be less than for a more dense rock of similar composition, if air fills pore spaces and lowers the magnitudes of the bulk dielectric constant and loss factor proportionally (assuming the ratio $\varepsilon''/\varepsilon'$ remains unchanged for each frequency under consideration).

B. Validity of a Dry Subsurface Model Assumption

Water content in rocks and sediments strongly affects the dielectric constant and loss factor. Dry rocks were assumed in this article; however, the subsurface environment on Mars is largely unknown and the presence of ice and brines in the near-surface could be possible, see, e.g., Stamenković *et al*. [1] and references within. Furthermore, the Phoenix lander measured diurnal variations in the dielectric constant at the surface, indicating possible atmospheric water uptake in the regolith [14] that could be consistent with a salty mixture in the ground affecting the dielectric properties over the course of a sol [67]. Perhaps GPR-imaging capabilities and penetration depths will change accordingly, which should be taken into concern during data interpretation, while also making it possible to study water exchange between the atmosphere and regolith through radar sounding.

Bound water in rocks and sediments, especially clays, is another potential aqueous source in Jezero, where phyllosilicate-signatures in VNIR-data indicate smectite carrying delta deposits. It has been hypothesized that bound water could be the reason behind the great radar loss experienced by space-borne radars orbiting Mars [79], in which case, an increased dielectric loss factor would be noticeable through sounding with RIMFAX. In accordance with measurements of Martian soil simulant JSC-1 [15], in this article bound water was included for the aeolian dunes and unconsolidated material, but only in thin surficial accumulations that did not distinctly affect imaging. If, however, high intrinsic attenuation would be detected over larger successions of smectite-rich delta deposits, radar sounding could turn out to be an appropriate tool for identifying and locating *in situ* water resources at the landing site.

V. Conclusion

A synthetic radargram was generated along a carefully selected acquisition traverse on the Jezero crater floor, enabling assessment of internal structures and detection of adjacent lithologies in a hypothesized geological setting. The modeling workflow shows the potential for assisting interpretation of data acquired on Mars by placing simulated radar sounding in the correct spatial context and by accurately estimating the returned signal levels. Comparing modeling results with actual RIMFAX-recordings could, therefore, help constrain subsurface geometries and electromagnetic properties. From orbital observations, uncertainties are ascribed stratigraphic relationships, lithological formations, as well as the electromagnetic properties of each geological unit; thus, decisive estimates of imaging capabilities are therefore not possible to make. Still, noticeable differences are expected between sounding over lava flows compared to tephra or volcanoclastic lithology, due to distinct internal structures and, in particular, due to how the low surface gravity on Mars affects sediment and rock generation and, consequently, the electromagnetic properties.

Acknowledgment

The authors would like to thank Geocap AS for granting an academic license for their software Geocap Desktop used in this research.

References

[1] V. Stamenković *et al.*, "The next frontier for planetary and human exploration," *Nat. Astron.,* vol. 3, no. 2, pp. 116–120, Jan. 2019.
[2] S. Hamran *et al.*, "Radar imager for mars' subsurface experiment.RIMFAX," in *Space Science Reviews*, vol. 216, no. 8, p. 128, 2020, doi: 10.1007/s11214-020-00740-4.
[3] B. Zhou *et al.*, "The subsurface penetrating radar on the rover of china's mars 2020 mission," in *Proc. 16th Int. Conf. Ground Penetrating Radar*, 2016. pp. 1–4.
[4] V. Ciarletti *et al.*, "WISDOM GPR designed for shallow and high-resolution sounding of the martian subsurface," *Proc. IEEE,* vol. 99, no. 5, pp. 824–836, May 2011.
[5] G. S. Baker and H. M. Jol, *Stratigraphic Analyses Using GPR*. Boulder, CO, USA: Geological Soc. Amer., 2007.
[6] J. K. Russell and M. V. Stasiuk, "Characterization of volcanic deposits with ground-penetrating radar," *Bull. Volcanol.,* vol. 58, no. 7, pp. 515–527, 1997.
[7] G. Olhoeft *et al.*, "Hot and cold lava tube characterization with ground penetrating radar," in *Proc. 8th Int. Conf. Ground Penetrating Radar*, 2000, pp. 482–487.
[8] G. Simmons *et al.*, "Surface electrical properties experiment," *Nat. Aeronaut. Space Admin.*, Washington, DC, USA, Apollo 17, Prelim. Sci. Rep. 330, 1973, p. 15.
[9] L. Xiao *et al.*, "A young multilayered terrane of the northern mare imbrium revealed by chang'E-3 mission," *Science,* vol. 347, no. 6227, 2015, Art. no. 1226.
[10] C. Li *et al.*, "The moon's farside shallow subsurface structure unveiled by chang'e-4 lunar penetrating radar," *Sci. Adv.,* vol. 6, no. 9, 2020, Art. no. eaay6898.
[11] M. J. Campbell and J. Ulrichs, "Electrical properties of rocks and their significance for lunar radar observations," *J. Geophysical Res.,* vol. 74, no. 25, pp. 5867–5881, 1969.
[12] G. R. Olhoeft and D. W. Strangway, "Dielectric properties of the first 100 meters of the moon," *Earth Planet. Sci. Lett.,* vol. 24, no. 3, pp. 394–404, Jan. 1975.
[13] F. T. Ulaby *et al.*, "Microwave dielectric properties of dry rocks," *IEEE Trans. Geosci. Remote Sens.,* vol. 28, no. 3, pp. 325–336, May 1990.
[14] A. Zent *et al.*, "Initial results from the thermal and electrical conductivity probe (TECP) on Phoenix," in *J. Geophysical Research: Planets.*, vol. 115, no. E3, 2010, doi: https://doi.org/10.1029/2009JE003420.
[15] D. Stillman and G. Olhoeft, "Frequency and temperature dependence in electromagnetic properties of martian analog minerals," *J. Geophysical Res., Planets,* vol. 113, no. E9, 2008, doi: 10.1029/2007JE002977.
[16] E. Heggy *et al.*, "Ground-penetrating radar sounding in mafic lava flows: Assessing attenuation and scattering losses in Mars-analog volcanic terrains," *J. Geophysical Res., Planets,* vol. 111, no. E6, 2006, doi: 10.1029/2005JE002589.
[17] R. E. Grimm *et al.*, "Absorption and scattering in ground-penetrating radar: Analysis of the bishop tuff," *J. Geophysical Res., Planets,* vol. 111, no. E6, 2006, doi: 10.1029/2005JE002619.
[18] R. B. Hargraves *et al.*, "The viking magnetic properties experiment: Primary mission results," *J. Geophysical Res.,* vol. 82, no. 28, pp. 4547–4558, 1977.
[19] S. F. Hviid *et al.*, "Magnetic properties experiments on the mars pathfinder lander: Preliminary results," *Science,* vol. 278, no. 5344, pp. 1768–1770, 1997.
[20] M. B. Madsen *et al.*, "Overview of the magnetic properties experiments on the mars exploration rovers," *J. Geophysical Res., Planets,* vol. 114, no. E6, 2009, doi: 10.1029/2008JE003098.
[21] B. Langlais *et al.*, "Crustal magnetic field of mars," *J. Geophysical Res., Planets,* vol. 109, no. E2, 2004, doi: 10.1029/2003JE002048.
[22] A. Mittelholz *et al.*, "The mars 2020 candidate landing sites: A magnetic field perspective," *Earth Space Sci.,* vol. 5, no. 9, pp. 410–424, 2018.

[23] G. Picardi *et al.*, "Radar soundings of the subsurface of mars," *Science,* vol. 310, no. 5756, 2005, Art. no. 1925.

[24] R. Seu *et al.*, "SHARAD sounding radar on the mars reconnaissance orbiter," *J. Geophysical Res., Planets,* vol. 112, no. E5, May 2007, doi: 10.1029/2006JE002745.

[25] G. A. Morgan *et al.*, "Radar investigations of the mars 2020 rover landing sites," in *Proc. 49th Lunar Planet. Sci. Conf.*, 2018, Paper 1404.

[26] T. A. Goudge *et al.*, "Assessing the mineralogy of the watershed and fan deposits of the jezero crater paleolake system, mars," *J. Geophysical Res., Planets,* vol. 120, no. 4, pp. 775–808, 2015.

[27] S. M. Cofield and K. M. Stack, "Geologic mapping and stratigraphic analysis of a candidate mars 2020 landing site: Jezero crater, mars," in *Proc. 49th Lunar Planet. Sci. Conf.*, 2018, Paper 2563.

[28] K. M. Stack *et al.*, "Photogeologic map of the perseverance rover field site in jezero crater constructed by the mars 2020 science team," in *Space Science Reviews*, vol. 216, no. 8, 2020, Art. no. 127, doi: 10.1007/s11214-020-00739-x.

[29] V. Z. Sun and K. M. Stack, "Understanding the continuity of regional units in the mars 2020 jezero and northeast syrtis regions: Implications for the origin of the mafic unit(s)," in *Proc. 50th Lunar Planet. Sci. Conf.*, 2019, Paper 2271.

[30] K. L. Tanaka *et al.*, "Assessment of planetary geologic mapping techniques for mars using terrestrial analogs: The SP mountain area of the san francisco volcanic field, arizona," *Planet. Space Sci.,* vol. 57, no. 5, pp. 510–532, May 2009.

[31] K. M. Stack *et al.*, "Comparing orbiter and rover image-based mapping of an ancient sedimentary environment, aeolis palus, gale crater, mars," *Icarus,* vol. 280, pp. 3–21, Dec. 2016.

[32] S. C. Schon *et al.*, "An overfilled lacustrine system and progradational delta in jezero crater, mars: Implications for noachian climate," *Planet. Space Sci.,* vol. 67, no. 1, pp. 28–45, Jun. 2012.

[33] B. H. N. Horgan *et al.*, "The mineral diversity of jezero crater: Evidence for possible lacustrine carbonates on mars," *Icarus*, vol. 339, Nov. 2019, Art. no. 113526.

[34] B. Wood *et al.*, "BGS groundhog desktop geoscientific information system external user manual," Brit. Geol. Survey, Nottingham, U.K., Rep. OR/15/046, 2015.

[35] C. Warren *et al.*, "gprMax: Open source software to simulate electromagnetic wave propagation for ground penetrating radar," *Comput. Phys. Commun.,* vol. 209, pp. 163–170, Dec. 2016.

[36] K. Yee, "Numerical solution of initial boundary value problems involving maxwell's equations in isotropic media," *IEEE Trans. Antennas Propag.,* vol. 14, no. 3, pp. 302–307, May 1966.

[37] K. S. Kunz and R. J. Luebbers, *The Finite Difference Time Domain Method for Electromagnetics*. Boca Raton, FL, USA: CRC Press, 1993.

[38] A. Taflove and S. C. Hagness, *Computational Electrodynamics: The Finite-Difference Time-Domain Method*. Norwood, MA, USA: Artech house, 2005.

[39] S. E. Hamran *et al.*, "Ground penetrating synthetic pulse radar: Dynamic range and modes of operation," *J. Appl. Geophys.,* vol. 33, no. 1, pp. 7–14, Jan. 1995.

[40] F. Uaby and D. Long, *Microwave Radar and Radiometric Remote Sensing*. Norwood, MA, USA: Artech House, 2015, pp. 201–203.

[41] S. C. Werner, "The early martian evolution—Constraints from basin formation ages," *Icarus,* vol. 195, no. 1, pp. 45–60, May 2008.

[42] C. I. Fassett and J. W. Head, "Sequence and timing of conditions on early mars," *Icarus,* vol. 211, no. 2, pp. 1204–1214, Feb. 2011.

[43] J. F. Mustard *et al.*, "Mineralogy of the nili fossae region with OMEGA/Mars express data: 1. Ancient impact melt in the isidis basin and implications for the transition from the noachian to hesperian," *J. Geophysical Res., Planets,* vol. 112, no. E8, 2007, doi: 10.1029/2006JE002834.

[44] J. F. Mustard *et al.*, "Composition, morphology, and stratigraphy of noachian crust around the isidis basin," *J. Geophysical Res., Planets,* vol. 114, no. E2, 2009, doi: 10.1029/2009JE003349.

[45] C. Fassett and J. W. Head, "Fluvial sedimentary deposits on mars: Ancient deltas in a crater lake in the nili fossae region," *Geophysical Res. Lett.,* vol. 32, no. 14, 2005.

[46] F. Poulet *et al.*, "Phyllosilicates on mars and implications for early martian climate," *Nature,* vol. 438, no. 7068, pp. 623–627, Dec. 2005.

[47] B. L. Ehlmann *et al.*, "Orbital identification of carbonate-bearing rocks on mars," *Science,* vol. 322, no. 5909, pp. 1828–1832, 2008.

[48] B. L. Ehlmann *et al.*, "Identification of hydrated silicate minerals on mars using MRO-CRISM: Geologic context near nili fossae and implications for aqueous alteration," *J. Geophysical Res., Planets,* vol. 114, no. E2, 2009, doi: 10.1029/2009JE003339.

[49] H. Hiesinger and J. W. Head, "The syrtis major volcanic province, mars: Synthesis from mars global surveyor data," *J. Geophysical Res., Planets,* vol. 109, no. E1, 2004, doi: 10.1029/2003JE002143.

[50] N. Barlow, "A review of martian impact crater ejecta structures and their implications for target properties," in *Large Meteorite Impacts III*, vol. 384. Boulder, CO, USA: Geological Soc. Amer., 2005, pp. 433–442.

[51] H. Dypvik *et al.*, "Mechanisms of late synimpact to early postimpact crater sedimentation in marine-target impact structures," in *Large Meteorite Impacts and Planetary Evolution IV*, vol. 465. Boulder, CO, USA: Geological Soc. Amer., 2010.

[52] H. Dypvik *et al.*, *Chesapeake Bay Impact Structure—Development of "Brim" Sedimentation in a Multilayered Marine Target*. Boulder, CO, USA: Geological Soc. Amer., 2018.

[53] J. B. Garvin *et al.*, "Craters on mars: Global geometric properties from gridded MOLA topography," in *Proc. 6th Int. Conf. Mars*, 2003, Paper 3277.

[54] B. L. Ehlmann *et al.*, "Clay minerals in delta deposits and organic preservation potential on mars," *Nat. Geosci.,* vol. 1, pp. 355–358, 2008.

[55] A. J. Brown *et al.*, "Olivine-carbonate mineralogy of the jezero crater region," *J. Geophysical Res., Planets,* vol. 125, no. 3, 2020, Art. no. e2019JE006011.

[56] L. Kah *et al.*, "Depositional relationships between crater floor materials in jezero crater, mars," in *Proc. 51st Lunar Planet. Sci. Conf.*, 2020, Paper 1301.

[57] T. A. Goudge *et al.*, "Constraints on the history of open-basin lakes on mars from the composition and timing of volcanic resurfacing," *J. Geophysical Res., Planets,* vol. 117, no. E12, 2012, doi: 10.1029/2012JE004115.

[58] S. Shahrzad *et al.*, "Crater statistics on the dark-toned, mafic floor unit in jezero crater, mars," *Geophysical Res. Lett.,* vol. 46, no. 5, pp. 2408–2416, 2019.

[59] C. I. Fassett and J. W. Head, "The timing of martian valley network activity: Constraints from buffered crater counting," *Icarus,* vol. 195, no. 1, pp. 61–89, May 2008.

[60] S. W. Ruff, "Investigating the floor of paleolake jezero by way of gusev crater," in *Proc. 4th Conf. Early Mars, Geologic, Hydrologic, Climatic Evol. Implic. Life*, 2017, Paper 3076.

[61] Mars 2020 Landing Site Working Group, "Mars 2020 science team assessment of jezero crater," in Presented at Fourth Landing Site Workshop for the Mars 2020 Rover Mission, [Online]. Available: https://marsnext.jpl.nasa.gov/workshops/2018-10/PRESENTATIONS/m2020_lsw_day2_19_Jezero_Final.pdf

[62] J. L. Dickson *et al.*, "A global, blended CTX mosaic of mars with vectorized seam mapping: A new mosaicking pipeline using principles of non-destructive image editing," in *Proc. 49th Lunar Planet. Sci. Conf.*, 2018, pp. 1–2.

[63] T. A. Goudge *et al.*, "Sedimentological evidence for a deltaic origin of the western fan deposit in jezero crater, mars and implications for future exploration," *Earth Planet. Sci. Lett.,* vol. 458, pp. 357–365, Jan. 2017.

[64] R. V. Morris *et al.*, "Identification of carbonate-rich outcrops on mars by the spirit rover," *Science,* vol. 329, no. 5990, pp. 421–424, 2010.

[65] S. M. Clifford, "A model for the hydrologic and climatic behavior of water on mars," *J. Geophysical Res., Planets,* vol. 98, no. E6, pp. 10973–11016, 1993.

[66] S. Piqueux *et al.*, "Widespread shallow water ice on mars at high latitudesand midlatitudes," *Geophysical Res. Lett.,* vol. 46, no. 24, pp. 14290–14298, 2019.

[67] D. E. Stillman and R. E. Grimm, "Dielectric signatures of adsorbed and salty liquid water at the phoenix landing site, mars," *J. Geophysical Res., Planets,* vol. 116, no. E9, Sep. 2011, doi: 10.1029/2011JE003838.

[68] L. M. Carter *et al.*, "Dielectric properties of lava flows west of ascraeus mons, mars," *Geophysical Res. Lett.,* vol. 36, no. 23, 2009, doi: 10.1029/2009GL041234.

[69] D. Jerram, "Volcanology and facies architecture of flood basalts," *Special Paper Geological Soc. Am,* vol. 362, pp. 119–132, Jan. 2002.

[70] S. Self *et al.*, "Emplacement of continental flood basalt lava flows," *Large Igneous Provinces, Continental, Ocean., Planet. Flood Volcanism*, vol. 100, pp. 381–410, Jan. 1997.

[71] K. W. Lewis *et al.*, "A surface gravity traverse on mars indicates low bedrock density at gale crater," *Science,* vol. 363, no. 6426, pp. 535–537, 2019.

[72] J. P. Grotzinger *et al.*, "Curiosity's mission of exploration at gale crater, mars," *Elements,* vol. 11, no. 1, pp. 19–26, 2015.

[73] H. J. Moore and B. M. Jakosky, "Viking landing sites, remote-sensing observations, and physical properties of martian surface materials," *Icarus,* vol. 81, no. 1, pp. 164–184, 1989.
[74] D. L. Sahagian and J. E. Maus, "Basalt vesicularity as a measure of atmospheric pressure and palaeoelevation," *Nature,* vol. 372, no. 6505, pp. 449–451, Dec. 1994.
[75] L. S. Crumpler, "MER field observations and analysis of vesicles in the gusev plains: Significance as records of emplacement environment," in *Proc. 36th Lunar Planet. Sci. Conf.*, 2005, Art. no. 2122.
[76] A. Rust and J. Russell, "Detection of welding in pyroclastic flows with ground penetrating radar: Insights from field and forward modeling data," *J. Volcanol. Geothermal Res.,* vol. 95, no. 1/4, pp. 23–34, 2000.
[77] S. L. Quane and J. K. Russell, "Ranking welding intensity in pyroclastic deposits," *Bull. Volcanol.,* vol. 67, no. 2, pp. 129–143, 2005.
[78] L. M. Carter *et al.*, "Shallow radar (SHARAD) sounding observations of the medusae fossae formation, mars," *Icarus,* vol. 199, no. 2, pp. 295–302, Feb. 2009.
[79] D. E. Stillman and R. E. Grimm, "Radar penetrates only the youngest geological units on mars," *J. Geophysical Res., Planets,* vol. 116, no. E3, 2011, doi: 10.1029/2010JE003661.

Sigurd Eide received the M.Sc. degree in geophysics, in 2014, from the University of Oslo, Norway, where he is currently working toward the Ph.D. degree in geophysics.

From 2014 to 2018, he was a Consultant within Marine Geophysics and Geographical Information Systems. His research interest include remote sensing and numerical modeling applied to geological exploration, in particular ground-penetrating radar and active-source seismic.

Svein-Erik Hamran received the M.Sc. degree in physics from the Norwegian University of Science and Technology, Trondheim, Norway, in 1984 and the Ph.D. degree in physics from the University of Tromø, Tromsø, Norway, in 1990.

He is currently a Professor with the Department of Technology Systems, University of Oslo. He is also the Principal Investigator of the Radar Imager for Mars subsurface eXperiment RIMFAX on the NASA Mars 2020 Perseverance Rover Mission and a Coprincipal Investigator on the WISDOM GPR experiment on the ESA ExoMars rover. His research interests include UWB radar design, radar imaging, and modeling in medical and ground-penetrating radar.

Henning Dypvik was born in Oslo, Norway. He received the Dr.philos. degree in geology from the University of Oslo, Norway, in 1985.

He is currently a Professor of Sedimentology and Petroleum geology with the University of Oslo. He has worked with field sedimentology and diagenetic analysis, in addition to detailed shale geochemistry. For the last 20 years, he has been involved in impact cratering and involved in the discoveries of the three Norwegian impact craters. His research interests include postimpact sedimentation.

Hans E. F. Amundsen received the M.Sc. and Ph.D. degree in volcanology and geochemistry from the University of Oslo, Norway, in 1987 and 1991, respectively.

He is currently a Geologist and the CEO with Vestfonna Geophysical AS, Kabelvåg, Norway. He is also a Long-Term Planner on Mars2020, Co-I on the RIMFAX GPR (Mars2020), and Co-I on the WISDOM GPR (ExoMars). His research interests include the are of scientific expertise covers volcanology, igneous- and sediment geochemistry, geochronology, organic geochemistry, development of rovers, payload instruments and planetary protection protocols, field geology and image analyses, sedimentology and basin evolution, and interpretation of seismic and electromagnetic data in subsurface imaging.